Urban-scale SALSCS, Part I: Experimental Evaluation and Numerical Modeling of a Demonstration Unit

Qingfeng Cao[1], Thomas H. Kuehn[1], Lian Shen[1], Sheng-Chieh Chen[2], Ningning Zhang[3], Yu Huang[3], Junji Cao[3**], David Y.H. Pui[1,4*]

[1] *Department of Mechanical Engineering, University of Minnesota, Minneapolis, Minnesota 55455, USA*
[2] *Department of Mechanical and Nuclear Engineering, Virginia Commonwealth University, Richmond, Virginia 23284, USA*
[3] *Key Lab of Aerosol Chemistry & Physics, Institute of Earth Environment, Chinese Academy of Sciences, Xi'an, Shaanxi 710061, China*
[4] *School of Science and Engineering, Chinese University of Hong Kong, Shenzhen, Guangdong 518172, China*

ABSTRACT

A demonstration unit for the Solar-Assisted Large-Scale Cleaning System (SALSCS), with a solar collector 43×60 m^2 in horizontal dimensions and a tower 60 m in height, was built in Xi'an, China, to study its effectiveness in terms of urban air pollution remediation. To simulate an urban-scale SALSCS with dimensions ranging 10–120 m that was proposed for installation on urban blocks, we first performed experimental measurements on the demonstration unit and used the experimental data to validate a numerical model that we developed. This paper presents the field measurements conducted during three days in Jan. 2017 in Xi'an. The experimental and numerical results of the system flow rate and temperature showed good agreement for six of the eight measurement cases, with average discrepancies of 1.63 m^3 s^{-1} for the flow rate and 0.78°C for the temperature. Larger discrepancies for the other two cases were observed, and the reasons were analyzed. During the measurements, the filtration efficiency of the filter media installed in the north section of the system with regard to PM$_{2.5}$ was evaluated to be 73.5%. The validated numerical model was applied to study the performance characteristics of the urban-scale SALSCS, and these results will be presented in Part II.

Keywords: SALSCS demonstration unit; Air pollution remediation; Experimental measurement; Model validation; Solar chimney.

INTRODUCTION

In recent years, many urban regions of the world have been suffering from severe air pollution due to the rapid economic expansions and industrial development (Mage *et al.*, 1996; Monks *et al.*, 2009; Fuzzi *et al.*, 2015; Baklanov *et al.*, 2016). Recently, the Solar-Assisted Large-Scale Cleaning System (SALSCS) was proposed by Cao *et al.* (2015) as a novel strategy to combat air pollution for urban regions. It utilizes renewable solar energy to generate updraft airflow, which shares the same working principle with the Solar Chimney (SC) system. Instead of applying

turbines to convert the kinetic energy of the airflow into electric energy as a Solar Chimney Power Plant (SCPP), SALSCS utilizes the system airflow to remove air pollutants in the atmosphere through filters. According to Cao *et al.* (2015), a full-scale SALSCS with system dimension on the order of kilometer was proposed to be installed in surrounding suburb regions of a city. Computational Fluid Dynamics (CFD) analysis were conducted for the system geometry and its volumetric airflow rate was estimated to be 2.64×10^5 m^3 s^{-1} after pressure drop of filters was considered in the numerical model.

To evaluate the capability of the full-scale SALSCS in removing urban air pollution, atmospheric simulations over the terrain of Beijing, China, have been performed by Cao *et al.* (2018) by using the Weather Research and Forecasting (WRF) model, where eight full-scale units were installed in the suburb along the 6th Ring Road of the city. It was found that 11.2% (or 14.6%) of PM$_{2.5}$ pollutants over the Beijing urban area were reduced by the eight systems with an operating flow rate of 2.64×10^5 m^3 s^{-1} (or 3.80×10^5 m^3 s^{-1}), where PM$_{2.5}$ is defined as fine particulate

---

* Corresponding author.
 Tel.: +1 6126252537; Fax: +1 6126256069
 E-mail address: dyhpui@umn.edu
** Corresponding author.
 Tel.: +86 029 62336261
 E-mail address: jjcao@ieecas.cn

matter in air less than 2.5 µm (Pui *et al.*, 2014).

In this paper, we propose to further improve SALSCS's efficiency of urban air pollution remediation by reducing the system geometric dimensions. This will allow for installation of multiple SALSCSs directly inside city blocks of urban regions. As a counterpart of the full-scale SALSCS, we define systems with solar collector and tower dimensions between 10 m and 120 m as urban-scale SALSCS. Fig. 1 presents a schematic diagram of the system, which is composed of the same four basic components as the full-scale unit, including a solar collector with transparent roof, a tower, filters and fans for generating more airflow. Air underneath the solar collector is heated by solar irradiation to have a lower density than the outside ambient air. Accordingly, buoyant updraft airflow is generated inside the SALSCS. Polluted atmospheric air flows in through the inlets on the four sides of the solar collector, and air pollutants are collected by filters. Afterwards, clean air is emitted from the tower outlet into the nearby urban atmosphere. The urban-scale SALSCS should have a solar collector of rectangular geometry so that it can easily fit into the city blocks, and its tower can be either a cylinder or vertical rectangular prism as long as the geometry matches the aesthetics of the nearby buildings.

The idea of using the SALSCS geometry to create airflow with the assistance of solar irradiation was inspired by the SC system. Detailed reviews of the SC technology were found to be presented by multiple researchers (Zhou *et al.*, 2010; Al-Kayiem and Aja, 2016; Kasaeian *et al.*, 2017). The first prototype of SC in the world was built in Manzanares, Spain, and it operated for nine years during which updraft airflow was generated consistently within the system (Haaf *et al.*, 1983; Haaf, 1984). From then, many researchers have conducted investigations on SC by theoretical, numerical and experimental approaches. Pasumarthi and Sherif (1998a, b) developed a mathematical model to evaluate the

performance of SC and performed experimental research on a demonstration model with a solar collector 18.3 m in diameter and 7.92 m in height. The major findings were that air temperature inside the system could be increased by extending the solar collector area and mass flow rate could be enhanced by installing an intermediate canvas absorber. Two-dimensional numerical simulations were conducted by Pastohr *et al.* (2004) for the geometry of the Manzanares prototype in Spain. The obtained numerical results showed good agreement with the analytical solutions derived from a simple model. Pretorius and Kröger (2006) utilized the numerical model developed by Pastohr *et al.* (2004) to study effects of various factors on the system performance, such as convective heat transfer coefficients, turbine inlet loss coefficient, glass roof quality of the solar collector and soil type. Ming *et al.* (2008) performed two-dimensional numerical simulations for the same Spanish prototype while considering the ground as an energy storage layer underneath the solar collector. A porous media model was applied to simulate the storage layer and influence of solar irradiation on the system performance was evaluated. Fasel *et al.* (2013) conducted both two- and three-dimensional numerical simulations on SCPP to investigate analytical scaling laws, and high-resolution numerical results of the flow and temperature fields were obtained. Guo *et al.* (2015) incorporated a radiation model and solar load model with a turbine resolved into a three-dimensional numerical model. The major conclusions were that the turbine rotational speed has different effects on turbine efficiency and system power output, and hourly variation of the sunlight zenith angle should be considered to better predict the system's performance. Gholamalizadeh and Kim (2016) performed CFD analysis on an SCPP with inclined collector roof, and found that a proper collector-roof inclination increases the system's performance in generating mass flow rate and providing higher power output. Recently, a new SCPP with radial partition walls in the solar collector was proposed by Ming *et al.* (2017). Three-dimensional model was developed and the numerical results showed that the radial partition walls improved the system performance and ambient cross-wind had negative effects on its performance. Recently, Ahmed and Patel (2017) performed both numerical and experimental studies on an SCPP prototype built on a Pacific island of Fiji, which had a collector diameter of 3.2 m and chimney height of 4 m. The experimental system was designed and optimized based on detailed numerical results, and system performance was evaluated under different solar irradiation and atmospheric wind speeds. The author concluded that the system airflow rate was increased by the atmospheric wind, water bags on the solar collector ground could reduce the fluctuations in power output for a diurnal cycle, and system air velocity and ground temperature had a linear relationship with the solar irradiation. A prototype of SC was set up by Maia *et al.* (2017) with a solar collector 25 m in diameter and a chimney 12.3 m in height. Ambient conditions and system airflow parameters were measured to perform a thermodynamic analysis on the drying process of bananas under the solar collector. Fathi *et al.* (2018) proposed a novel idea of combining
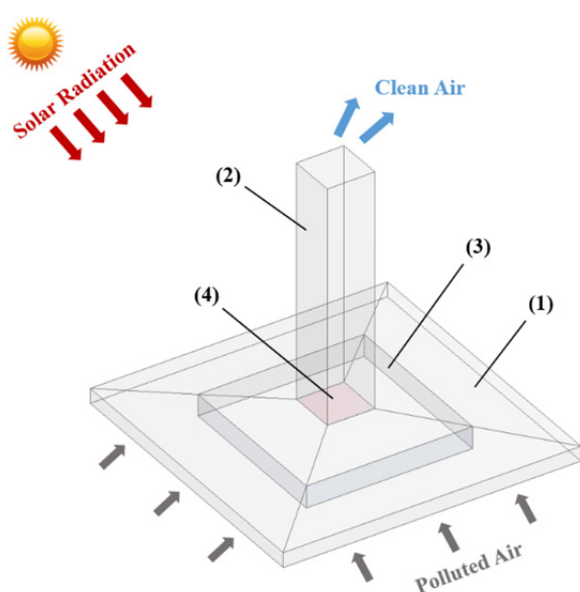

Fig. 1. Schematic diagram of an urban-scale SALSCS with (1) solar collector, (2) tower, (3) filters, and (4) fans (optional).

SCPP with nuclear power plant to improve the efficiency of SCPP in generating electric power, where SCPP functions as a cooling tower of the nuclear power plant. A pilot system with same chimney height and collector diameter of 3 m was investigated by Fadaei *et al.* (2018) to find out effects of latent heat storage of the ground on the system performance. According to the study, the paraffin wax as a phase-change material with higher latent heat storage capability applied on the ground improved the airflow generation and overall performance of the system. However, no SC prototype has yet been reported with a solar collector or tower dimension larger than 50 m, except for the Manzanares system operated in the 1980s.

A demonstration unit of the urban-scale SALSCS was constructed in the city of Xi'an, China, with a unique design in that its solar collector was divided by partition walls into four sections installed with different filters, allowing each section to operate individually. The system has a solar collector 43×60 m^2 in horizontal dimensions and a tower 60 m in height, which is larger than most SC prototypes presented in literature. Detailed description of the system will be given in the following section. The current investigation is aimed to perform field measurements on the airflow field of the demonstration unit and apply the experimental data to validate a numerical model developed for the urban-scale SALSCS. This paper first presents a detailed description of the Xi'an demonstration unit, and then discusses methods of the field measurements and numerical simulations on the urban-scale SALSCS. In the "Results and discussion" section, comparisons of the system flow rates and the temperatures from the experimental data and numerical results are presented as a validation of the numerical model. A parametric study on the urban-scale SALSCS by using the validated numerical model will be introduced in Part II of this paper for understanding effects of various ambient and geometric parameters on system performance.

XI'AN DEMONSTRATION UNIT OF SALSCS

Construction of the demonstration unit of SALSCS was completed around July of 2016, which is located near the Shaanxi Normal University in the southern area of the Xi'an city in China. Fig. 2(a) shows a schematic diagram of the system (drawn to scale). It has a rectangular solar collector (1) with a dimension of 43 m in the east–west direction and 60 m in the north–south direction, and a tower (2) with a height and diameter of 60 m and 10 m, respectively. The collector height increases from 3.4 m at the system inlet to 5.5 m at the observation balcony (7) next to the base of the tower. The balcony has a horizontal dimension of 16×16 m^2. As indicated by Fig. 2(a), the solar collector is divided into four sections by partition walls (4), while at the outlet of each collector section, a rolling door (6) was installed. In this way, each section of the system can operate either individually or together with the other sections by manipulating the rolling doors. Three different filters (3) were installed at the mid-way interfaces of the three sections in the north, west and east directions,

so that the filtration performance on PM$_{2.5}$ of the filters can be tested. The filter media in the west section is manufactured by Donaldson Company, Inc., the one in the east is a domestic filter and in the north section is the High Air Flow (HAF) air filter manufactured by the 3M company. The one section on the south of the solar collector was left open, which was considered to be a good setup to validate our numerical model of SALSCS developed in the ANSYS Fluent fluid solver, as this section receives the most solar irradiation among the four sections during daytime, which contributes to the strongest airflow field within the solar collector. Since the solar collector area of the west and east sections are smaller than the other two sections, fans are installed behind the rolling doors of the two sections to generate more flow rate, in case that the flow fields in the two sections were not strong enough to pass through the installed filters. The numerical simulation work presented in this paper was only conducted on the south and north sections of the Xi'an SALSCS, where effects of fans on the system flow field need not to be considered. Four storerooms (5) were also constructed at the base of the observation balcony for storing experimental facilities.

Fig. 2(b) presents a photo of the Xi'an SALSCS during daytime. As indicated by the figure, part of the tower and solar collector support was painted by red color for decoration. The solar collector was covered by glass materials while the tower and balcony was constructed with concrete. The ground of the solar collector was covered by a mixture of cobblestone and sand to store heat during daytime and release heat for the system operation at night. At the edge of the solar collector in the north and south sections, two clusters of solar panels were installed to test their efficiency in generating electricity, which was designed to drive the system fans together with electricity from the city power grid. Fig. 2(c) shows a photo of the unit at night when the decorative lights are on. The Xi'an demonstration unit locates in a busy area of the southern part of the city where many buildings and new apartments nearby are under construction. The system has been working consistently to generate airflow with the help of solar energy in daytime and thermal energy stored in the ground underneath at night, as long as the rolling doors are left open. It demonstrates that the configuration of SALSCS (or SC) is a good approach for airflow generation with the buoyancy principle by utilizing the renewable solar energy. SALSCS takes advantage of the generated airflow to realize PM$_{2.5}$ removal purpose by filters, while SCPP converts the kinetic energy of airflow to electricity by turbines.

EXPERIMENTAL MEASUREMENT

Measurement Instrumentation

Experimental measurements were conducted on the Xi'an demonstration unit to mainly evaluate the system flow rate and validate the numerical model. Different system parameters were measured under conditions with zero ambient wind velocity to exclude the effect of ambient wind on its performance during both experiments and simulations. During each measurement, airflow velocity and temperature
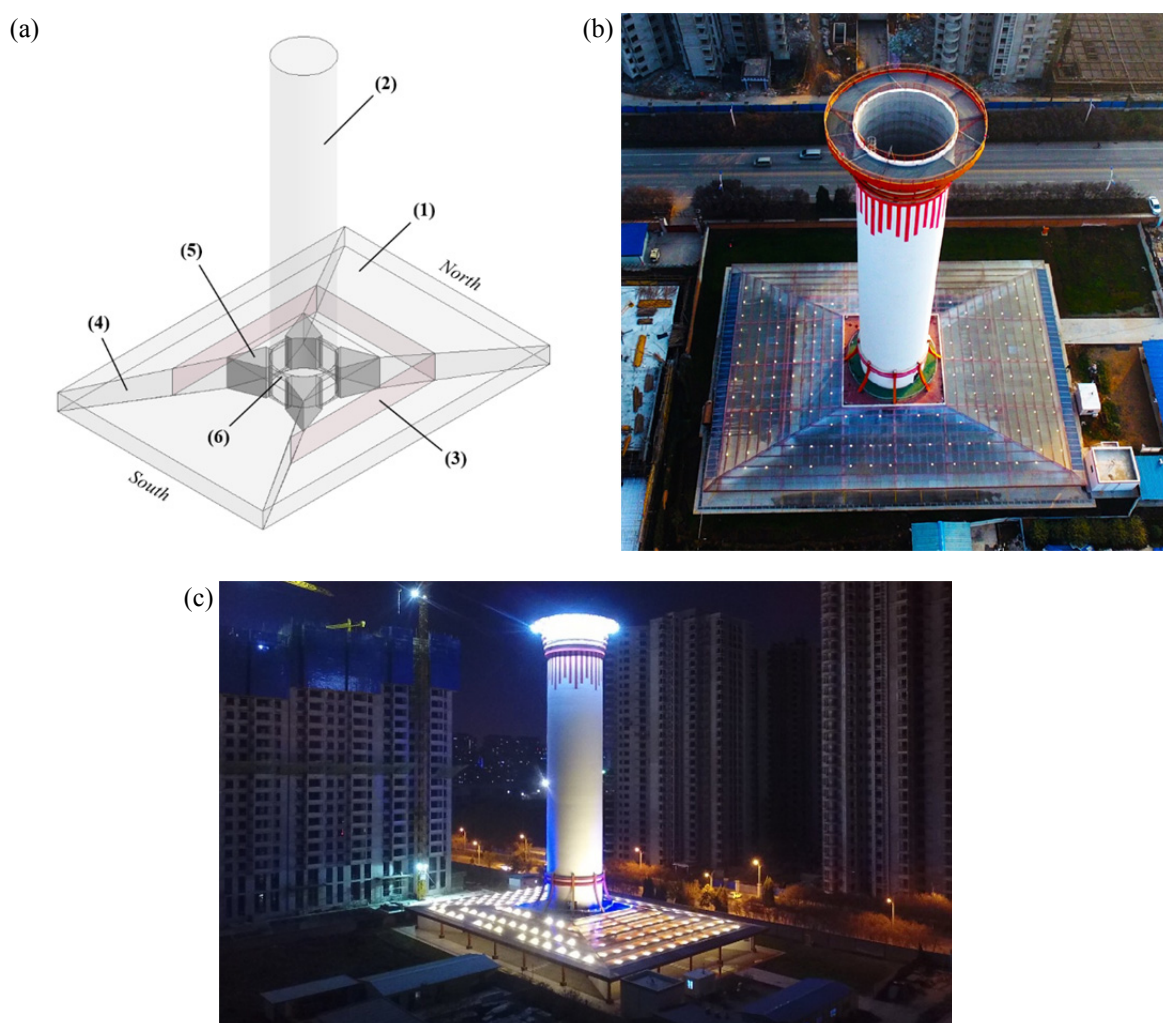
(a)

(b)

(c)

Fig. 2. Xi'an demonstration unit of SALSCS. (a) Schematic diagram of the demonstration unit (drawn to scale) with (1) solar collector, (2) tower, (3) filters, (4) partition walls, (5) storage room, and (6) rolling doors; (b) a picture of the Xi'an SASLCS taken during daytime; and (c) a picture of it with decorative lighting at night.

were measured within the SALSCS demonstration unit. Ambient parameters were recorded at the same time, which includes atmospheric pressure, temperature, and intensity of solar irradiation.

A Gill WindSonic portable wind sensor was applied to measure the airflow speed inside the SALSCS at different locations, which has both air velocity and direction as its outputs. It has a measurement range of 0–60 m s^{-1} with a resolution of 0.01 m s^{-1}. The accuracy of flow velocity measurements with the Gill WindSonic sensor is ±2% (at 12 m s^{-1}). A Kestrel 4000 portable weather meter was chosen to measure the temperature inside the system. The weather meter measures parameters under normal weather conditions with an accuracy of ±1°C for temperature. Parameters of the ambient environment, including ambient temperature, atmospheric pressure, wind speed (which was chosen to be zero for the current study) and solar irradiation, were monitored and downloaded together from a MAWS201 automatic weather station installed on the roof of a small building next to the SALSCS site with a height of about 3 m above the ground. The temperature sensor of

the weather station has a measurement range of –40–60°C with an accuracy of ±0.2°C. The pressure sensor measures atmospheric pressure from 600 hPa to 1100 hPa with a resolution of 0.1 hPa and a measurement accuracy of ±0.3 hPa. The wind speed sensor of MAWS201 has a measurement range of 0.5–60 m s^{-1} and accuracy of ±0.3 m s^{-1} (≤ 10 m s^{-1}) or error less than 2% (> 10 m s^{-1}). As discussed later, the numerical boundary condition applied at the bottom of the SALSCS solar collector requires the measurement data of ambient solar irradiation. The solar irradiation sensor on MAWS201 measures solar irradiation intensity with a measurement range of –2000–2000 W m^{-2} and error of < ±2% per year under operating temperature between –30°C and 70°C. A DustTrack DRX Handheld Aerosol Monitor 8534 was also utilized to measure the PM$_{2.5}$ concentrations at different locations inside the SALSCS or in the nearby regions outside the system to test the filtration efficiency of PM$_{2.5}$ in the filters installed inside the northern section. The aerosol monitor has a measurement range of 0.001–150 mg m^{-3} and accuracy of ±5% under operational temperature of 0–50°C.

Experimental Method for Measuring System Flow Rate and Temperature

The experimental measurements presented in this paper were only performed on the south and north sections of the Xi'an SALSCS, which are respectively the open section and the section installed with the HAF air filter. It has a lower airflow resistance (pressure drop) than normal filters, so that the airflow velocity can be maintained at a higher value. Since the north section generates airflow only by solar energy without fans, the low pressure drop across the HAF filters is helpful for the system to maintain the consistent airflow. By only evaluating the open and HAF sections of the system, we avoided the impact of fans on the flow field, making it easier for our numerical model of the SALSCS demonstration unit which will be validated against the measurement data. Our experiments were conducted under three SALSCS operation conditions, which are:

A. Only the open (south) section was operating;
B. Only the HAF (north) section was operating;
C. Both the two sections were operating together.

During each measurement, the airflow velocity, its direction and temperature within the solar collector in the south and (or) north sections of the system were recorded. For the flow velocity, measurement data were taken from two measurement surfaces within the system solar collector, which are at the rolling-door location of the solar collector outlet and the mid-way interface between the solar collector inlet and the tower center, respectively, as shown in Fig. 3. Theoretically, the two mass flow rate values should be equal according to the law of mass conservation. During our measurements, the average of the mass flow rate values across the two measurement surfaces was considered as the final measured system mass flow rate for each section. Figs. 4(a)–4(b) presents the dimensions of the two measurement surfaces and layouts of the measurement points at the two locations which are indicated by the black dots. The rolling-door surface has a dimension of 3.75 × 4.20 m^2 with 20 measurement points, and the mid-way

interface has a dimension of 25.60 × 4.30 m^2 with a total of 84 measurement points. The airflow velocity parameter was measured point by point according to the layout configuration. In the numerical model, we assumed that the data set of each measurement case was collected at the same time, so that the input air properties of the model were assumed to be all constants based on the ambient temperature. However, under real experimental situations, it took some time to complete each measurement data set, since the measurements were conducted point by point, and meanwhile, the angle and intensity of the sunlight, atmospheric temperature and pressure vary with time consistently during the daytime. Therefore, each set of measurements should be conducted both accurately and efficiently. To reduce measurement time, the parameter of flow temperature was measured only at the rolling-door surface with 20 measurement points during the experiments. The representative temperature at this collector outlet location was calculated as the average of the measured temperature values of all the measurement points. For filtration efficiency evaluation, PM$_{2.5}$ concentrations were also measured at the upstream and downstream locations of the HAF filter in the north section, while the ambient PM$_{2.5}$ concentration outside of the SALSCS was also recorded at different location near the Xi'an SALSCS. For each location, we took the concentration data for multiple times, and used the average value as the final PM$_{2.5}$ concentration data. It took about 20–30 minutes to complete the data collection procedure for each experimental case.

System flow rate is a critical parameter to evaluate SALSCS's ability to generate updraft airflow and to clean polluted atmospheric air through its filters. It is also the first parameter that should be considered to validate our numerical model developed using the ANSYS Fluent software. In this study, the total volumetric flow rate in each SALSCS section is calculated as the sum of the product of airflow velocity at each measurement point and the corresponding surface area as illustrated by Fig. 4(a), which is described by the following equation:

$$\dot{V} = \sum_i u_i A_i \,, \tag{1}$$

where V is the calculated volumetric system flow rate, u_i is the wind speed normal to the rolling-door surface at measurement point i, and A_i is the corresponding surface area indicated by the shadow area in Fig. 4(a) whose dimensions are presented accordingly. The summation terms in Eq. (1) are estimates of the volumetric flow rates passing through each measurement surface under a certain system operational condition.

NUMERICAL MODEL OF THE XI'AN DEMONSTRATION UNIT

A numerical model of the demonstration unit was developed using ANSYS Fluent version 17.0 (ANSYS, 2016). Modeling conditions, including system dimensions and input ambient parameters, were set to be same as the

Fig. 3. A photo showing measurement surfaces where measurement data were taken. Background of the photo are buildings under construction at the surrounding region of the demonstration unit.
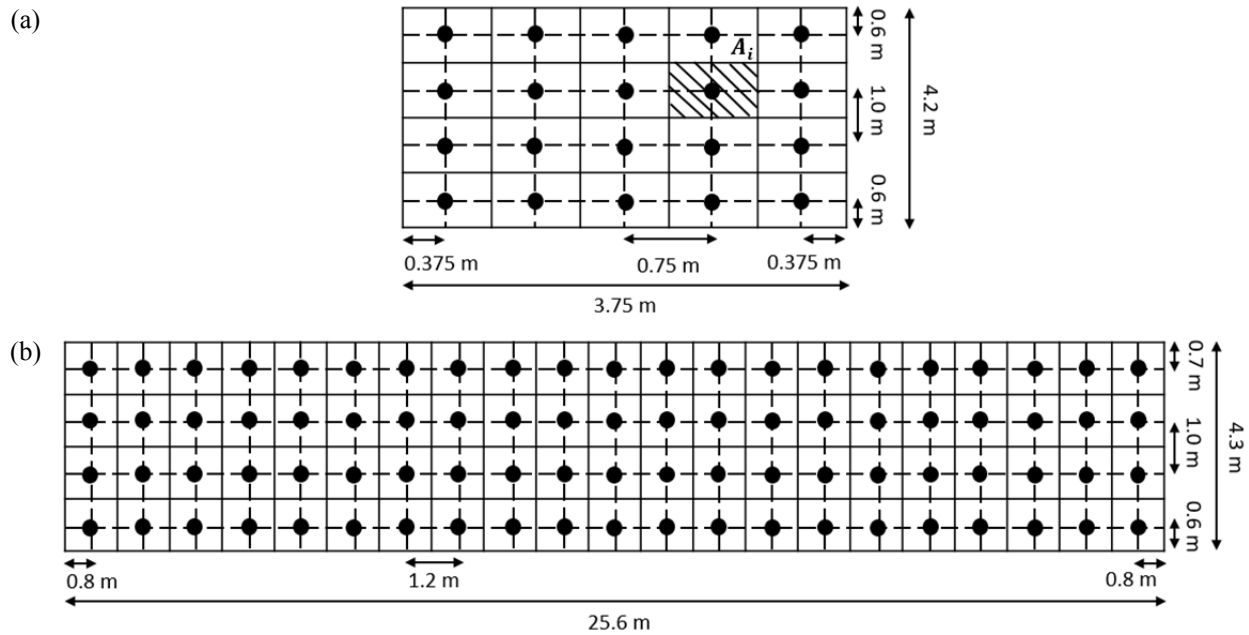
(a)

(b)

Fig. 4. Layout of the measurement points at (a) the rolling-door inside the SALSCS and (b) the mid-way interface between the collector inlet and the tower center.

geometry of the demonstration unit and measured ambient conditions, respectively, in order to validate our numerical model against the measurement data. Air properties in the model were chosen to be related to the corresponding ambient temperature. For the buoyancy-driven flow (natural convection) in SALSCS, the Rayleigh number, Ra, is applied to characterize the laminar to turbulent transition. It is defined as the product of the Grashof number, Gr, and the Prandtl number, Pr. The latter two numbers are given by, respectively:

$$\mathrm{Gr} = \frac{g\beta\left(T_{\max} - T_{\min}\right)L^3}{v^2}, \tag{2}$$

$$\mathrm{Pr} = \frac{v}{\alpha}, \tag{3}$$

where g is the gravitational acceleration, β is the thermal expansion coefficient, calculated for an ideal gas as the reciprocal of the absolute temperature, L is the characteristic length equal to the solar collector height or tower diameter, v is the kinematic viscosity, and α is the thermal diffusivity. $T_{\max}$ and $T_{\min}$ in Eq. (2) are the maximum and minimum temperatures of the system airflow, respectively. Transition from laminar to turbulent flow happens when Ra is around 10^9. The actual Ra number obtained in this study is larger than 10^{10} under all simulation conditions, indicating that the flow field within the Xi'an demonstration unit of SALSCS is turbulent.

Governing Equations

To simulate the buoyancy-driven flow inside the Xi'an SALSCS, we assumed the flow field to be incompressible

with Boussinesq approximation applied, which states that the variation of air density in the flow field is only important in the buoyancy term multiplied by the gravitational acceleration, g, of the momentum equation, and can be neglected in the rest of the equation (Spiegel and Veronis, 1960; Gray and Giorgini, 1976). The buoyancy term, F, is simplified to be proportional to the temperature difference between the local temperature, T, and the operating temperature, T_0, and is written as:

$$F_i = -\rho\beta(T - T_0)g_i, \tag{4}$$

where ρ is the constant density of the flow, and the thermal expansion coefficient, β, is calculated as $1/T_0$ here. In this way, the flow in SALSCS is treated to be incompressible in our numerical model, and meanwhile, all the parameters of air properties are set to be constant under the operating temperature.

The three-dimensional Reynolds-averaged Navier–Stokes (RANS) equations were chosen to solve the mean velocity field for the turbulent flow within the system. Based on the Reynolds decomposition of the flow field, the mean velocity is defined as

$$\langle u_i \rangle = u_i - u_i', \tag{5}$$

where the local velocity, u_i, is decomposed into its mean, $\langle u_i \rangle$, and the velocity fluctuation, u_i'. Governing equations for the conservation of mass, momentum, and energy are given in Eqs. (6)–(8), respectively.

Continuity equation:

$$\frac{\partial \langle u_i \rangle}{\partial u_i} = 0. \tag{6}$$

Momentum equations:

$$\frac{\partial \langle u_i \rangle}{\partial t} + \langle u_j \rangle \frac{\partial \langle u_i \rangle}{\partial x_j} = \nu \frac{\partial^2 \langle u_i \rangle}{\partial x_j \partial x_j} - \frac{\partial \langle u_i' u_j' \rangle}{\partial x_j} - \frac{1}{\rho} \frac{\partial \langle p \rangle}{\partial x_i} + \frac{F_i}{\rho}. \tag{7}$$

Energy equation:

$$\frac{\partial \langle T \rangle}{\partial t} + \langle u_j \rangle \frac{\partial \langle T \rangle}{\partial x_j} = \alpha \frac{\partial^2 \langle T \rangle}{\partial x_j \partial x_j} - \frac{\partial \langle u_j' T' \rangle}{\partial x_j}, \tag{8}$$

where α is the thermal diffusivity, and Reynolds decomposition of the temperature field, T, gives:

$$T = <T> + T'. \tag{9}$$

Here $<T>$ is the mean temperature, and T' is the temperature fluctuation. The Reynolds stress, $<u_i'u_j'>$, in Eq. (7), and the temperature flux, $<u_j'T'>$, in Eq. (8), give the closure problem of the governing equations for turbulent flows (Pope, 2000). In the current study, they were modeled by Eqs. (10) and (11) based on the turbulent-viscosity and gradient-diffusion hypotheses, respectively,

$$\langle u_i' u_j' \rangle = \frac{2}{3} k \delta_{ij} - \nu_t \left(\frac{\partial \langle u_i \rangle}{\partial x_j} + \frac{\partial \langle u_j \rangle}{\partial x_i} \right), \tag{10}$$

$$\langle u_j' T' \rangle = \frac{\nu_t}{\sigma_T} \frac{\partial \langle T \rangle}{\partial x_j}, \tag{11}$$

where k is the turbulent kinetic energy, δ_{ij} is the Kronecker delta function, σ_T is the energy Prandtl number as a model constant, and ν_t is the turbulent viscosity. Thus, Eqs. (10) and (11) provide a convenient closure to the governing equations of Eqs. (6)–(8), as long as the turbulent viscosity is determined. In the current study, we chose to apply the k–ε two-equation turbulent model to determine ν_t, which is widely used as an economic approach to solve turbulent flow problems. For the two-equation turbulent model, the turbulent viscosity, ν_t, is related to the turbulent kinetic energy, k, and the turbulent kinetic energy dissipation rate, ε, and is specified as:

$$\nu_t = C_\mu k^2 / \varepsilon, \tag{12}$$

where C_μ is a model constant. The governing equations for k and ε are given by Eqs. (13) and (14), respectively.

Transport equation for turbulent kinetic energy, k:

$$\frac{\partial k}{\partial t} + \langle u_j \rangle \frac{\partial k}{\partial x_j} = \frac{\partial}{\partial x_j} \left[\left(\nu + \frac{\nu_t}{\sigma_k} \right) \frac{\partial k}{\partial x_j} \right] + P + \beta g_i \frac{\nu_t}{\sigma_T} \frac{\partial \langle T \rangle}{\partial x_i} - \varepsilon. \tag{13}$$

Transport equation for turbulent kinetic energy dissipation

rate, ε:

$$\frac{\partial \varepsilon}{\partial t} + \langle u_j \rangle \frac{\partial \varepsilon}{\partial x_j} = \frac{\partial}{\partial x_j} \left[\left(\nu + \frac{\nu_t}{\sigma_\varepsilon} \right) \frac{\partial \varepsilon}{\partial x_j} \right] + C_{\varepsilon 1} \frac{\varepsilon}{k} \left(P + C_{\varepsilon 3} \beta g_i \frac{\nu_t}{\sigma_T} \frac{\partial T}{\partial x_i} \right) - C_{\varepsilon 2} \frac{\varepsilon^2}{k}, \tag{14}$$

where σ_k and σ_ε are the Prandtl numbers for k and ε, respectively, and P represents the generation of turbulent kinetic energy due to the mean velocity gradients:

$$P = -\langle u_i' u_j' \rangle \frac{\partial \langle u_j \rangle}{\partial x_i}. \tag{15}$$

The model constants are given as $C_\mu = 0.09$, $C_{\varepsilon 1} = 1.44$, $C_{\varepsilon 2} = 1.92$, $\sigma_k = 1.0$, $\sigma_\varepsilon = 1.3$ and $\sigma_T = 0.85$ (ANSYS, 2016; Pope, 2000; Launder and Sharma, 1974). Determination of the model parameter, $C_{\varepsilon 3}$, can be referred to ANSYS Fluent user manual (ANSYS, 2016). Eqs. (6)–(8) and Eqs. (10)–(14) compose the governing equations that were solved for the flow and temperature fields inside the Xi'an demonstration unit.

Computational Domains and Boundary Conditions

The computational domains for the three SALSCS operation conditions during the experimental measurements are shown in Figs. 5(a)–5(c), with domain boundaries labeled in the figure. The only difference between the domains of Conditions A and B is that the latter has a HAF filter installed along the mid-way interface between the solar collector inlet and the tower centerline. In the numerical model, pressure drop, Δp, was applied at this interface to simulate the effect of the HAF filter on the flow field within the north section of the SALSCS, which is estimated as a function of the face velocity, v_F:

$$\Delta p = 4.39 v^2 + 5.20 v. \tag{16}$$

The coefficient in the above polynomial was obtained based on our experimental tests on the installed HAF filter media. Each computational domain is composed of two regions, the air region inside the system and a 2-m thick soil layer below the ground surface as indicated by the grey color region in Fig. 5. The soil layer was treated as pure solid and heat conduction happens in the layer. To simulate the solar heating effect, it was assumed that a heat source of 0.0001-m thickness on the ground surface releases heat flux into the computational domain with a value same as the measured ambient solar irradiation. Since the tower is constructed with concrete that blocks sunlight, the ground surface under the tower was assumed to release no heat flux into the domain. Temperature at the bottom of the 2-m soil layer was considered to be a constant 4°C higher than the corresponding ambient temperature, which is a typical ground temperature for the Xi'an region in the northern China during winter seasons. As will be mentioned
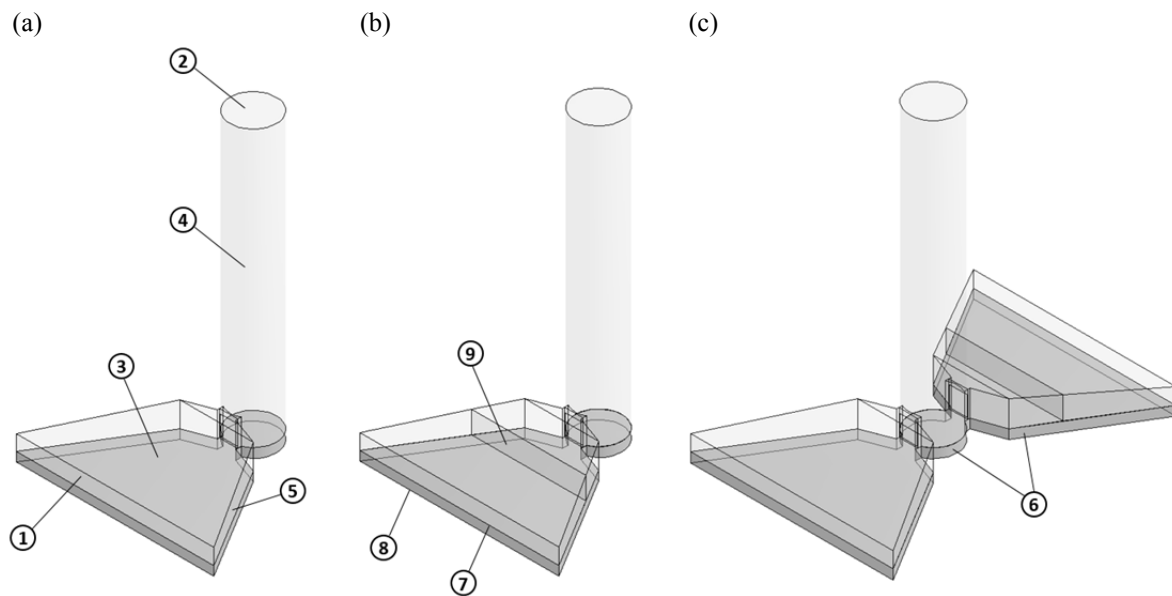
Fig. 5. Computational domains and boundary conditions for the three SALSCS operation conditions of (a) only the south section operating, (b) only the north section operating, and (c) both the two sections operating together. Domain boundaries are labeled by numbers and illustrated in Table 1.

in Section 6.2.1.3, a parametric study shows that it is a reasonable ground temperature for simulations of the demonstration unit. Convective heat transfer occurs between the solar collector roof and the above ambient air, where the convective heat transfer coefficient, h, was adopted from the study of Bernardes *et al.* (2007) for low ambient velocity. The ambient-air temperature, atmospheric pressure, and solar irradiation were assumed to be constants equal to the measured ambient data for each case. As the SALSCS tower is only 60 m, the pressure at both the collector entrance and tower exit are assumed equal to the measured atmospheric pressure. The no-slip boundary condition is applied at all the wall-type boundaries of the three computation domains. Since the tower wall and partition walls are built by concrete, they are assumed to be adiabatic. The boundary conditions of the numerical model are summarized in Table 1.

Meshing Strategy

A hexahedron dominant meshing strategy was employed for our model as an economic approach. As shown in Fig. 6, most parts of the computational domain were discretized with structured grids, while unstructured grids were applied only at few parts of the solar collector to adopt for the irregular geometry. At the near-wall regions of the solar collector and tower, grids are refined in order to improve the computational accuracy with the standard wall function chosen to model the unresolved near-wall flow field. As indicated by Fig. 6(b), finer structured grids were applied at the connection area between the collector and the tower to minimize errors from the complex flow field at this location.

Grid-independent studies were performed to determine if the chosen total grid number affects the numerical results significantly. Three simulation cases with total grid

numbers of 1,791,987 (Case A), 3,587,072 (Case B) and 5,416,302 (Case C) were tested, respectively. The simulation condition for the test cases was chosen to be the same as measurement Case 1 as given in Table 2, where the measurement was conducted on the south section of the SALSCS with only one section operating. Fig. 7 presents the grid-independence performance of our model. By changing the grid number from Case A to Case C, the discrepancies are only 0.769 m^3 s^{-1} in volumetric flow rate and 0.021 K in the average temperature at the tower outlet, respectively, indicating that our model has an excellent grid-independence performance. Thus, the grid number of Case B (3,587,072) was chosen for the current study. To model the different geometry under SALSCS Operational Condition C when both the two sections were operating together, the grid spacing and distribution were kept the same as the test Case B, but the total grid number was increased accordingly.

Computational Method

The ANSYS Fluent fluid solver employs the finite volume method for solving the governing equations presented in Section 4.1. The pressure-based solver was applied for the incompressible flow. SIMPLE algorithm was chosen as the pressure-velocity coupling scheme, and body-force-weighted algorithm was selected as the pressure interpolation scheme. Advection and diffusion terms in the governing equations were discretized by the second-order scheme. Considering the geometry of the Xi'an SALSCS demonstration unit has various length scales, the double precision solver was applied to carry out the numerical calculations in this study. The absolute convergence criteria were set to be 10^{-6} for all the variables to monitor the solution convergent performance of the numerical simulations.

Table 1. Boundary conditions for the numerical model of the Xi'an demonstration unit.

Location	Boundary type	Value
1. Solar collector inlet	Pressure inlet Constant temperature	Ambient pressure and temperature [a]
2. Tower outlet	Pressure outlet	Ambient pressure [a]
3. Solar collector roof	No-slip boundary Convective heat transfer with the ambient environment	$h = 8$ W m^{-2} K^{-1}; Ambient temperature [a]
4. Tower wall	No-slip boundary Adiabatic	$q = 0$ W m^{-2}
5. Partition walls	No-slip boundary Adiabatic	$q = 0$ W m^{-2}
6. Side surface of the soil layer	Adiabatic	$q = 0$ W m^{-2}
7. Ground surface	No-slip boundary Constant heat flux	Ambient solar irradiation [a]
8. Bottom surface of the soil layer	Constant temperature	4 degrees higher than ambient temperature [a]
9. Filter	Pressure drop as a function of face velocity	Δp calculated by Eq. (16).

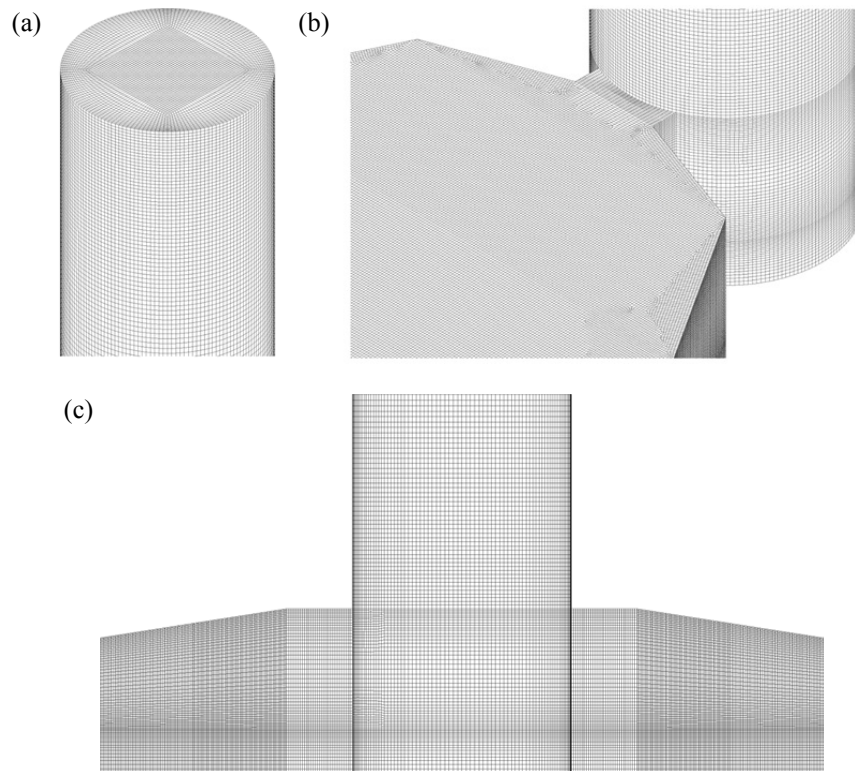[a] Data referring to the measured ambient parameters in Table 2.

Fig. 6. Meshing distribution of the numerical model for Xi'an Demonstration Unit: (a) grid distribution near the tower outlet, (b) grid distribution near the solar collector outlet, and (c) grid distribution near the tower bottom region.

Because of the large grid number, parallel computing was performed for our simulations on the Itasca High-Performance Computing (HPC) platform of the Minnesota Supercomputing Institute (MSI) to expedite the numerical calculations. The Itasca platform has 8 processor cores per computational node, and we typically used 16 nodes (128 cores in total) with 2300 MB of RAM per processor core for each numerical simulation. Each calculation took about 1.5–3 hours.
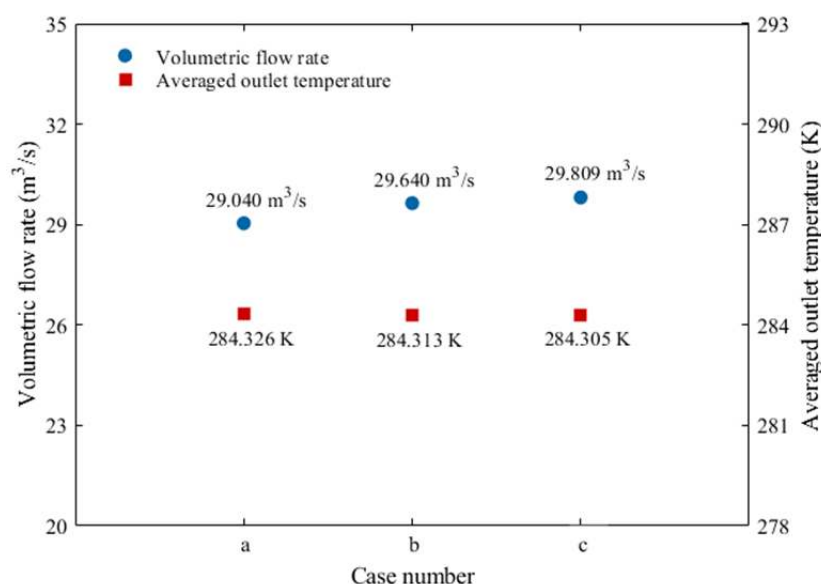
RESULTS AND DISCUSSION

Measurement Results for Ambient Conditions

Experimental measurements on the demonstration unit of SALSCS were conducted for three consecutive days in Xi'an, China, from Jan. 11 to Jan. 13, 2017. As presented in Table 2, there were in total eight experimental cases studied. The measurement data include ambient solar irradiation, temperature, atmospheric pressure and the time

Table 2. Ambient data recorded during the experimental measurements for the demonstration unit of SALSCS in Xi'an, China.

Operation conditions	Case number	Measured section	Measurement time (Local Beijing time)	Solar irradiation (W m^{-2})	Ambient temperature (°C)	Ambient pressure (hPa)
Only one section operated	1	South section	Jan. 13 2:52 pm–3:20 pm	100.9	9.6	968.3
	2	South section	Jan. 13 10:10 am–10:35 am	166.2	3.9	972.6
	3	North section	Jan. 13 11:10 am–11:37 am	246.9	6.6	971.9
Both sections operated	4	South section	Jan. 11 11:17 am–11:44 am	108.7	4.6	978.5
	5	South section	Jan. 12 10:48 am–11:39 am	262.7	6.8	975.5
	6	North section				
	7	South section	Jan. 13 4:03 pm–4:58 pm	33.4	9.0	968.0
	8	North section				

Fig. 7. Grid-independence study of the numerical model. The study was carried out under the condition of measurement Case 1 in Table 2. Here Cases a, b and c indicate total grid numbers of 1,791,987; 3,587,072; and 5,416,302, respectively.

period (local Beijing time) for each measurement. Table 2 also shows that either one of the open (south) or HAF (north) sections or both of them were operated for each experimental case, and the system flow rate and temperature values of the two sections were evaluated separately. We chose to carry out the experiments under conditions when there was no ambient wind speed to exclude influence of the wind velocity on system performance in generating airflow field. On Jan. 11, the cloud coverage was high, and therefore, the solar irradiation and ambient temperature values were fairly low even at noon time. For the next two days, the cloud coverage was low during the entire day, but moderate air pollution could be observed within the surface layer of the atmosphere, especially for Jan. 13. From 4:00 to 5:00 p.m. on Jan. 13 was close to the time of sunset, so that a low solar irradiation value was observed. The measured average ambient pressure for the eight cases

at the SALSCS location is 972.5 hPa. The recorded ambient parameters during our experimental measurements provide input data for the numerical model for comparisons between the experimental measurements and the numerical simulations.

Measurement Results for PM$_{2.5}$ Concentrations

PM$_{2.5}$ concentrations of the ambient environment near the SALSCS, and at the upstream and downstream locations of the HAF filter of the north section were measured, respectively. As presented in Table 3, except for Case 1 and 2, we recorded the concentration data during six of the eight measurement cases, during which the north section was operating. From Jan. 11 to Jan. 13, ambient PM$_{2.5}$ concentrations gradually increased from 33 µg m^{-3} to 60.9 µg m^{-3}. Table 3 indicates that the measured upstream concentration was almost equal to the ambient

Table 3. Measurement data of PM$_{2.5}$ concentrations and filtration efficiency of the HAF filter media in the north section of the Xi'an demonstration unit with regards to PM$_{2.5}$.

Measurement time [b] (Local Beijing time)	Case number(s) [b]	Solar irradiation [b] (W m^{-2})	Ambient PM$_{2.5}$ concentration (µg m^{-3})	Upstream PM$_{2.5}$ concentration (µg m^{-3})	Downstream PM$_{2.5}$ concentration (µg m^{-3})	Filtration efficiency of HAF filter
Jan 13 11:10 am–11:37 am	3	246.9	66.2	69.5	20.2	70.9
Jan 11 11:17 am–11:44 am	4	108.7	33.0	31.7	6.9	78.2
Jan 12 10:48 am–11:39 am	5 & 6	262.7	42.6	42.3	15.5	63.4
Jan 13 4:03 pm–4:58 pm	7 & 8	33.4	60.9	65.3	12.0	81.6

[b] Data corresponding to Table 2.

data for all the experimental cases, while the downstream concentration was significantly lower than the other two concentrations because of the cleaning effect of the HAF filter. Filtration performance of a filter can be evaluated by the filtration efficiency, defined as

$$E = \frac{C_{up} - C_{down}}{C_{up}} \qquad (17)$$

where C_{up} and C_{down} are the upstream and downstream PM$_{2.5}$ concentrations of the filter, respectively. Table 3 shows that the HAF filtration efficiency increases as the ambient solar irradiation decreases. Higher solar irradiation generates stronger airflow field, which increases the face velocity of the filters and, consequently, reduces the filter's performance. In average, the measured filtration efficiency of the HAF filter in the north section of the demonstration unit is 73.5%. To be noted here, the ion generators of the HAF filters were not turned on during our three-day measurements. With the ion generators operating, the filtration efficiency can be improved significantly. More detailed studies on performance evaluation of the filters installed in the Xi'an demonstration unit will be covered in future publications.

Comparison between Measurement Data and Numerical Results

Fig. 8 presents the comparison of numerically predicted and experimentally measured volumetric system flow rates and solar collector outlet temperatures obtained from both the numerical calculations and experimental measurements, respectively. Except for Cases 3 and 6, the average absolute discrepancies of the numerical results from the experimental data are 1.63 m^3 s^{-1} for the system flow rate and 0.78°C for the temperature at the solar collector outlet, respectively, indicating that our numerical results agree well with the measurement data. For Cases 3 and 6, the numerical results of both the system flow rate and temperature at the solar collector outlet are significantly higher than the experimental data. The larger discrepancies for the two cases, which on average are 16.5 m^3 s^{-1} and 3.21°C for the flow rate and the temperature, respectively, are mainly due to that the

solar energy received by the north section during the sunny morning-to-noon measurement time was much smaller than the solar irradiation data measured by the weather station installed on the roof of the small building next to the SALSCS. Shadows of the tower, partition walls and other opaque structures of the system in the north section blocked away a large amount of incoming sunlight, causing a much smaller solar irradiation value received by the ground of the north section collector than the measured ambient solar irradiation which was applied as an actual input for the numerical simulations. The presented comparisons between the numerical results and experimental data serve as a validation for the numerical model developed by using the ANSYS Fluent fluid solver, which was applied for the parametric investigation on the urban-scale SALSCS.

SUMMARY

To remediate urban air pollution, installing a large number of urban-scale Solar-Assisted Large-Scale Cleaning Systems (SALSCSs), which possess both a solar collector and a tower with dimensions between 10 and 120 m, on city blocks has been proposed. This paper evaluates a demonstration unit in Xi'an, China, built with a 43 × 60 m^2 solar collector—uniquely separated into four sections by walls—and a 60 m tower, and introduces approaches to field measurements and numerical simulations using the ANSYS Fluent fluid solver. Experimental measurements were conducted during three days in Jan. 2017, and data about the system flow rate and the temperature at the solar collector outlet were recorded under different operating conditions. The numerical results agreed well with the experimental data, showing that for six of the eight measurement cases, the average discrepancies were 1.63 m^3 s^{-1} and 0.78°C for the flow rate and the outlet temperature, respectively. Larger differences for the other two cases were observed, which was caused by the fact that the measured ambient solar irradiation did not accurately represent the actual energy received by the solar collector in the north section due to the tower and the partition walls, which blocked sunlight to the north section during the sunny portion of the day. The filtration efficiency for PM$_{2.5}$ of the HAF filter media installed in the north section
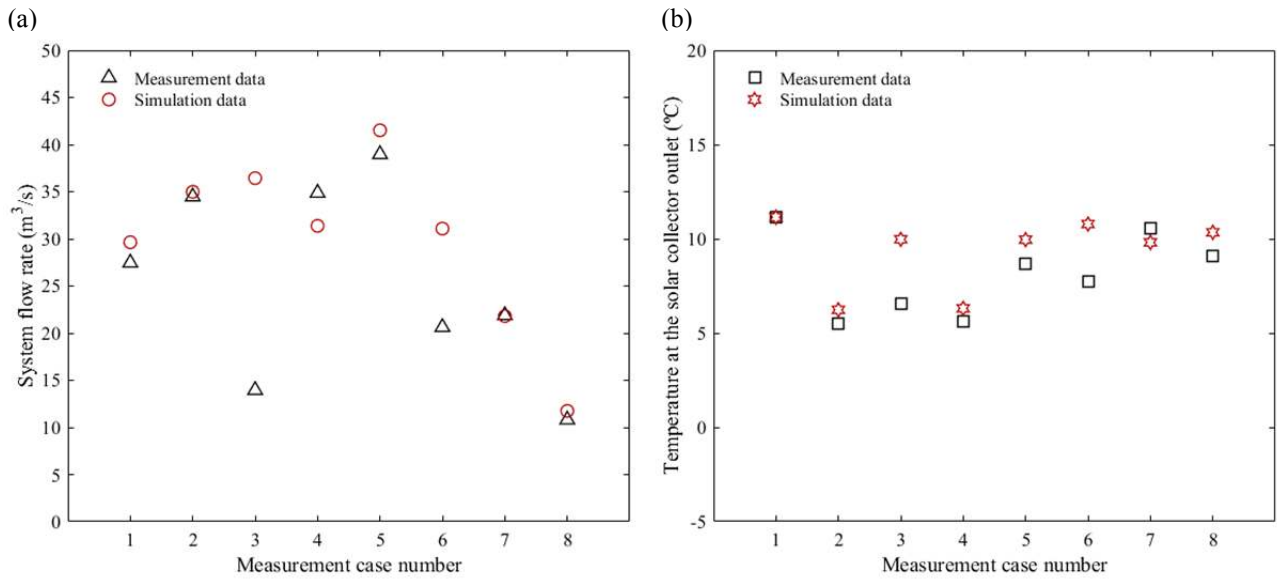
(a)

(b)

Fig. 8. Comparison of numerical and experimental results for the eight measurement cases for (a) system flow rate and (b) temperature at the outlet of the solar collector.

of the solar collector was evaluated to be 73.5% on average. The comparable results for the system flow rate and the temperature validate the numerical model we developed for the urban-scale SALSCS, which was in turn used to investigate the effects of various geometric dimensions and ambient variables on system performance. A detailed parametric study will be presented in Part II of this paper.

NOMENCLATURE

A	surface area corresponding to each measurement point, m^2
C	PM$_{2.5}$ concentration, $\mu g\ m^{-3}$
$C_\mu, C_{\varepsilon 1}, C_{\varepsilon 2}, C_{\varepsilon 3}$	constants for turbulent model
E	filtration efficiency of PM$_{2.5}$ in filter media, %
F	buoyancy term in the momentum equation, $kg\ m^{-2}\ s^{-2}$
Gr	Grashof number
g	gravitational acceleration, $m\ s^{-2}$
h	convective heat transfer coefficient, $W\ m^{-2}\ K^{-1}$
k	turbulent kinetic energy, $m^2\ s^{-2}$
L	characteristic length, m
P	generation of turbulent kinetic energy due to the mean velocity gradient, $m^2\ s^{-3}$
p	pressure, Pa
p_0	reference pressure, 10^5 Pa
Pr	Prandtl number
q	heat flux, $W\ m^{-2}$
Ra	Rayleigh number
T	temperature, K
T_0	operating temperature, K
$<T>$	mean temperature, K
T'	temperature fluctuation, K
u	velocity component, $m\ s^{-1}$
$<u>$	mean velocity, $m\ s^{-1}$
u'	velocity fluctuation, $m\ s^{-1}$
$\dot{V}$	volumetric system flow rate, $m^3\ s^{-1}$
v	face velocity across filter media, $m\ s^{-1}$

Greek

α	thermal diffusivity, $m^2\ s^{-1}$
β	thermal expansion coefficient, K^{-1}
δ	Kronecker delta
ε	turbulent kinetic energy dissipation rate, $m^2\ s^{-3}$
Δp	pressure drop across filter media, Pa
v	kinematic viscosity, $m^2\ s^{-1}$
v_t	turbulent viscosity, $m^2\ s^{-1}$
ρ	air density, $kg\ m^{-3}$
σ_ε	turbulent Prandtl number for k
σ_k	turbulent Prandtl number for ε
σ_T	energy Prandtl number

Subscripts

down	downstream of filter media
i	subscript index

j	subscript index
max	maximum
min	minimum
up	upstream of filter media

REFERENCES

Ahmed, M.R. and Patel, S.K. (2017). Computational and experimental studies on solar chimney power plants for power generation in Pacific island countries. *Energy Convers. Manage.* 149: 61–78.

Al-Kayiem, H.H. and Aja, O.C. (2016). Historic and recent progress in solar chimney power plant enhancing technologies. *Renewable Sustainable Energy Rev.* 58: 1269–1292.

ANSYS (2016). ANSYS fluent 17.0 theory guide. ANSYS, Inc.

Baklanov, A., Molina, L.T. and Gauss, M. (2016). Megacities, air quality and climate. *Atmos. Environ.* 126: 235–249.

Bernardes, M.A.S., von Backström, T.W. and Kröger, D.G. (2007). Critical evaluation of heat transfer coefficients applicable to solar chimney power plant collectors. Proceedings of ISES Solar World Congress Conference, Beijing, China, pp. 1706–1713.

Cao, Q., Pui, D.Y.H. and Lipiński, W. (2015). A concept of a novel solar-assisted large-scale cleaning system (SALSCS) for urban air remediation. *Aerosol Air Qual. Res*. 15: 1–10.

Cao, Q., Shen, L., Chen, S.C. and Pui, D.Y.H. (2018). WRF modeling of $PM_{2.5}$ remediation by SALSCS and its clean air flow over Beijing terrain. *Sci. Total Environ*. 626: 134–146.

Fadaei, N., Kasaeian, A., Akbarzadeh, A. and Hashemabadi, S.H. (2018). Experimental investigation of solar chimney with phase change material (PCM). *Renewable Energy* 123: 26–35.

Fasel, H.F., Meng, F., Shams, E. and Gross, A. (2013) CFD analysis for solar chimney power plants. *Sol. Energy* 98: 12–22.

Fathi, N., McDaniel, P., Aleyasin, S.S., Robinson, M., Vorobieff, P., Rodriguez, S. and de Oliveira, C. (2018). Efficiency enhancement of solar chimney power plant by use of waste heat from nuclear power plant. *J. Cleaner Prod.* 180: 407–416.

Fuzzi, S., Baltensperger, U., Carslaw, K., Decesari, S., Denier van der Gon, H., Facchini, M.C., Fowler, D., Koren, I., Langford, B., Lohmann, U., Nemitz, E., Pandis, S., Riipinen, I., Rudich, Y., Schaap, M., Slowik, J.G., Spracklen, D.V., Vignati, E., Wild, M., Williams, M. and Gilardon, S. (2015). Particulate matter, air quality and climate: lessons learned and future needs. *Atmos. Chem. Phys*. 15: 8217–8299.

Gholamalizadeh, E. and Kim, M.H. (2016). CFD (Computational Fluid Dynamics) analysis of a solar-chimney power plant with inclined collector roof. *Energy* 107: 661–667.

Gray, D.D. and Giorgini, A. (1976). The validity of the Boussinesq approximation for liquids and gases. *Int. J.*

Heat Mass Transfer 19: 545–551.

Guo, P., Li, J., Wang, Y. and Wang, Y. (2015). Numerical study on the performance of a solar chimney power plant. *Energy Convers. Manage.* 105: 197–205.

Haaf, W. (1984). Solar chimneys, Part II: Preliminary test results from the Manzanares pilot plant. *Int. J. Solar Energy* 2: 141–161.

Haaf, W., Friedrich, K., Mayr, G. and Schlaich, J. (1983). Solar chimneys, Part I: Principle and construction of the pilot plant in Manzanares. *Int. J. Solar Energy* 2: 3–20.

Kasaeian, A.B., Molana, S., Rahmani, K. and Wen, D. (2017). A review on solar chimney systems. *Renewable Sustainable Energy Rev.* 67: 954–987.

Launder, B.E. and Sharma, B.I. (1974). Application of the energy-dissipation model of turbulence to the calculation of flow near a spinning disc. *Lett. Heat Mass Transfer* 1: 131–138.

Mage, D., Ozolins, G., Peterson, P., Webster, A., Orthofer, R., Vandeweerd, V. and Gwynne, M. (1996). Urban air pollution in megacities of the world. *Atmos. Environ*. 30: 681–686.

Maia, C.B., Ferreira, A.G., Cabezas-Gómez, L., de Oliveira Castro Silva, J. and de Morais Hanriot, S. (2017). Thermodynamic analysis of the drying process of bananas in a small-scale solar updraft tower in Brazil. *Renewable Energy* 114: 1005–1012.

Ming, T., Liu, W., Pan, Y. and Xu, G. (2008). Numerical analysis of flow and heat transfer characteristics in solar chimney power plants with energy storage layer. *Energy Convers. Manage.* 49: 2872–2879.

Ming, T., Wu, Y., de_Richter, R.K., Liu, W. and Sherif, S.A. (2017). Solar updraft power plant system: A brief review and a case study on a new system with radial partition walls in its collector. *Renewable Sustainable Energy Rev.* 69: 472–487.

Monks, P.S., Granier, C., Fuzzi, S., Stohl, A., Williams, M.L., Akimoto, H., Amann, M., Baklanov, A., Baltensperger, U., Bey, I., Blake, N., Blake, R.S., Carslaw, K., Cooper, O.R., Dentener, F., Fowler, D., Fragkou, E., Frost, G.J., Generoso, S., Ginoux, P., Grewe, V., Guenther, A., Hansson, H.C., Henne, S., Hjorth, J., Hofzumahaus, A., Huntrieser, H., Isaksen, I.S.A., Jenkin, M.E., Kaiser, J., Kanakidou, M., Klimont, Z., Kulmala, M., Laj, P., Lawrence, M.G., Lee, J.D., Liousse, C., Maione, M., McFiggans, G., Metzger, A., Mieville, A., Moussiopoulos, N., Orlando, J.J., O'Dowd, C.D., Palmer, P.I., Parrish, D.D., Petzold, A., Platt, U., Pöschl, U., Prévôt, A.S.H., Reeves, C.E., Reimann, S., Rudich, Y., Sellegri, K., Steinbrecher, R., Simpson, D., ten Brink, H., Theloke, J., van der Werf, G.R., Vautard, R., Vestreng, V., Vlachokostas, Ch. and von Glasow, R. (2009). Atmospheric composition change – global and regional air quality. *Atmos. Environ*. 43: 5268–5350.

Pastohr, H., Kornadt, O. and Gürlebeck, K. (2004). Numerical and analytical calculations of the temperature and flow field in the upwind power plant. *Int. J. Energy Res*. 28: 495–510.

Pasumarthi, N. and Sherif, S.A. (1998a). Experimental and theoretical performance of a demonstration solar chimney

model – Part I: Mathematical model development. *Int. J. Energy Res*. 22: 277–288.

Pasumarthi, N. and Sherif, S.A. (1998b). Experimental and theoretical performance of a demonstration solar chimney model – Part II: Experimental and theoretical results and economic analysis. *Int. J. Energy Res*. 22: 443–461.

Pope, S.B. (2000). *Turbulent flows*, Cambridge University Press, Cambridge, U.K.

Pretorius, J.P. and Kröger, D.G. (2006). Critical evaluation of solar chimney power plant performance. *Sol. Energy* 80: 535–544.

Pui, D.Y.H., Chen, S.C. and Zuo, Z. (2014). PM$_{2.5}$ in China: Measurements, sources, visibility and health Effects, and mitigation. *Particuology* 13: 1–26.

Spiegel, E.A. and Veronis, G. (1960). On the Boussinesq approximation for a compressible fluid. *Astrophys. J.* 131: 442–447.

Zhou, X., Wang, F. and Ochieng, R.M. (2010). A review of solar chimney power technology. *Renewable Sustainable Energy Rev.* 14: 2315–2338.